



A graphical user interface (GUI) for model-based radiation-induced acoustic computed tomography

Michelle Simon^{*,**}, Prabodh Kumar Pandey^{†,§,||,**}, Leshan Sun^{*}
and Liangzhong Xiang^{*,†,‡,¶,||}

**Department of Biomedical Engineering
Samueli School of Engineering, University of California
Irvine, CA 92617, USA*

*†Department of Radiological Sciences
School of Medicine, University of California
Irvine, CA 92697, USA*

*‡Beckman Laser Institute & Medical Clinic
University of California
Irvine, CA 92612, USA*

*§pkpandey@hs.uci.edu; prabodhphyee@gmail.com
¶liangzhx@hs.uci.edu*

Received 14 September 2022

Accepted 15 December 2022

Published 6 February 2023

Radiation-induced acoustic computed tomography (RACT) is an evolving biomedical imaging modality that aims to reconstruct the radiation energy deposition in tissues. Traditional back-projection (BP) reconstructions carry noisy and limited-view artifacts. Model-based algorithms have been demonstrated to overcome the drawbacks of BPs. However, model-based algorithms are relatively more complex to develop and computationally demanding. Furthermore, while a plethora of novel algorithms has been developed over the past decade, most of these algorithms are either not accessible, readily available, or hard to implement for researchers who are not well versed in programming. We developed a user-friendly MATLAB-based graphical user interface (GUI; RACT2D) that facilitates back-projection and model-based image reconstructions for two-dimensional RACT problems. We included numerical and experimental X-ray-induced acoustic datasets to demonstrate the capabilities of the GUI. The developed algorithms support parallel computing for evaluating reconstructions using the cores of the computer, thus further accelerating the reconstruction speed. We also share the MATLAB-based codes for evaluating RACT reconstructions, which users with MATLAB programming expertise can further modify to suit their needs. The shared GUI and codes can be of interest to researchers across the globe and assist them in efficient evaluation of improved RACT reconstructions.

^{||}Corresponding authors.

^{**}These authors contributed equally to this work.

Keywords: Radiation-induced acoustic computed tomography (RACT); image reconstruction; graphical user interface (GUI); photoacoustic tomography.

1. Introduction

Radiation-induced acoustic computed tomography (RACT) is a noninvasive imaging technique that uses radiation (such as X-ray,^{1–8} laser,^{9–12} microwave,^{13–16} and ion^{17–20}) pulses to irradiate tissues and ultrasonic transducers to sense the resulting ultrasound (US) waves originated by the thermo-elastic expansion and contraction of the tissues. Transducers can be arranged in a variety of planar or volumetric arrays — i.e., linear, circular, and spherical — in accordance with the physical constraints of different imaging targets, granting a greater variety in clinical usage. The data generated by the transducers require substantial post-processing and analytical computation to produce the reconstructed maps of the energy deposition (ED) in the tissue.

Photoacoustic tomography (PAT)^{9–12} employs lasers for the excitation of the tissues and has been used to image soft tissues. However, due to the high optical scattering in tissues, the imaging depth of PAT is limited to a few centimeters.²¹ In contrast, owing to a significantly lower scattering, X-rays and ion beams can penetrate much deeper into the tissue. Therefore, X-ray-induced acoustic tomography (XACT)^{1–8} and proto-/iono-acoustic tomography (PrAT/IAT)^{17–20} image deeper into the tissue and have been researched extensively over the last 10 years. X-rays and proton beams are commonly used in clinical radiation therapy for cancer treatment where intense X-ray/ion beams are guided toward the tumor to destroy the malignant cells.^{22,23} Accurate dose delivery at the tumor site is crucial for the procedure’s success. The most commonly studied application of XACT and PrAT/IAT is *in-vivo* dose monitoring during radiation therapy.^{7,24–30} Research also shows the potential of XACT/PrAT/IAT for radiological biomedical imaging and non-destructive evaluation of materials.^{31–37}

Back-projections (BPs) are the most commonly used algorithm to evaluate reconstructions in RACT.^{1,38} A BP reconstruction is achieved by the cumulative addition of data from each detector back-projected based on the acoustic time of flight. The model-based (MB) algorithms facilitate

incorporating sound speed variations, finite aperture, sensor directivity, and regularizing priors. Studies in the literature on RACT^{39–41} demonstrate that MB algorithms reduce limited-view and noisy artifacts compared to the traditional BP algorithms. MB schemes are based on a model that relates the radiation energy deposition (RED) to the collected US signals. To reduce the computational demands associated with three-dimensional RACT, circular transducer arrays are commonly employed to collect the in-plane US waves which facilitates reconstruction of the two-dimensional RED map.^{39,42–52} MB reconstructions commonly require explicit computation and storage of the model-matrix, which is inefficient and demands huge computational memory for problems where high resolution is desired. MB reconstructions in the graphical user interface (GUI) were evaluated via the LSQR (least squares with QR-factorization) minimization function in MATLAB, which facilitates utilizing functions for on-the-run matrix-vector multiplications, thus circumventing the computation and storage of the measurement matrix. A computationally efficient, noniterative model-back-projection (MBP)⁴⁰ algorithm has also been included in the GUI, giving users the opportunity to compare the BP, MBP, and LSQR reconstructions side by side.

While several reconstruction algorithms for RACT have been developed by the researchers, there is a lack of open-source and easy to implement algorithms. *K*-wave toolbox²⁴ is the most used software for simulating US propagation and RACT reconstruction. There are some toolboxes^{53,54} for achieving multispectral photoacoustic image reconstruction. However, using these toolboxes requires significant coding expertise. Recently, Omidi *et al.* developed a MATLAB-based graphical package⁵⁵ for photoacoustic simulation and image reconstruction. However, this toolbox lacks the capability for model-based image reconstruction. To provide a convenient and quick apparatus for performing such reconstructions that can be used by technicians, doctors, and researchers alike, we have created a GUI capable of evaluating three 2D imaging

reconstructions: BP, MBP, and LSQR method. In addition to the multiple reconstruction methods, the GUI enables users to choose the reconstruction grid (size and grid resolution) and can perform user-directed signal filtering for improved imagery. It also provides users with the choice between Laplacian and Tikhonov regularization while evaluating the LSQR reconstructions. The GUI is capable of quick processing of photoacoustic data regardless of transducer location and offers the user a multitude of modifiable parameters for variable reconstructions. To the best of our knowledge, this is the first GUI for performing MB image reconstructions in RACT. We also share the MATLAB-based codes for evaluating RACT reconstructions, which users with MATLAB programming expertise can further modify to suit their needs. The GUI installer, codes, and the sample data have been uploaded on our website: <https://truelab.som.uci.edu/software/ract2d-toolbox/>.

The rest of this paper is structured as follows. Section 2 deals with the theory behind the radiation-induced US, the MB algorithm, and its implementation in the GUI. In Sec. 2, we also elaborate on the method used for creating the GUI, while the components of the GUI and their usage along with the datasets included in the GUI and the corresponding reconstruction results are discussed in Sec. 3. Concluding remarks are offered in Sec. 4.

2. Materials and Methods

2.1. Mathematical formulation

The radiation-induced acoustic waves propagation due to radiation energy deposition in the tissues is

defined by³⁸

$$\frac{\partial^2 p(\mathbf{r}, t)}{\partial t^2} - v^2 \nabla^2 p(\mathbf{r}, t) = \Gamma H(\mathbf{r}) \frac{\partial \delta(t)}{\partial t}, \quad (1)$$

where Γ is the Gruneisen parameter, v is the sound speed in tissue, and H is the RED map. The solution to Eq. (1) in a 2D problem setting can be expressed as³⁹

$$\begin{aligned} p(\mathbf{r}, t) &= \frac{\partial}{\partial t} \left(\frac{1}{vt} \int_{S(\mathbf{r}, t)} H(\mathbf{r}') v t d\theta \right) \\ &= \frac{\partial}{\partial t} \left(\int_{S(\mathbf{r}, t)} H(\mathbf{r}') d\theta \right), \quad |\mathbf{r} - \mathbf{r}'| = vt, \end{aligned} \quad (2)$$

where $S'(\mathbf{r}, t)$ represents a circular segment centered at a detector location \mathbf{r} and radius $|\mathbf{r} - \mathbf{r}'| = vt$ [Fig. 1(a)]. The detailed calculations demonstrating the construction of model-matrix M from Eq. (2) can be found in our earlier publication.³⁵ In the discrete domain, Eq. (2) can be written as

$$\underline{p} = M \underline{h}, \quad (3)$$

with M [size: $(N_d \cdot N_t) \times N$], \underline{p} [size: $(N_d \cdot N_t) \times 1$], and \underline{h} (size: $N \times 1$) being the model-matrix, discrete RA measurement vector, and discrete domain representation of the RED, respectively. Here, N_d and N_t are the total numbers of detectors and time samples, while N represents the total number of nodes in the discretized RED map. The RACT reconstruction problem is to compute the RED map (\hat{h}) from the RA measurement vector ($\underline{p}_{\text{meas}}$), which can be written as a regularized least-square (LS) optimization as follows^{39,40}:

$$\hat{h} = \arg \|\underline{p}_{\text{meas}} - M \underline{h}\|_2^2 + \lambda^2 \|\underline{h}\|_2^2, \quad (4)$$

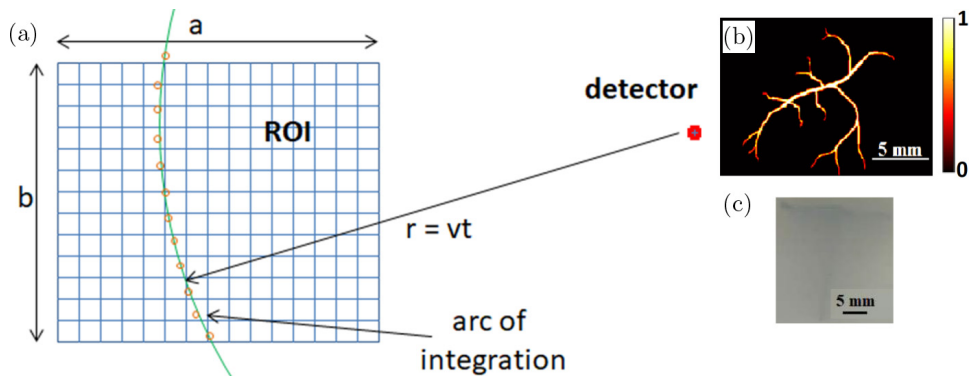


Fig. 1. (a) Arc for calculating the integral in Eq. (3) at time t , (b) the true vascular structure for which the numerical dataset has been generated, and (c) the photograph of the phantom for which XACT experimental measurements were collected and included with the GUI.

where $\|\cdot\|_2$ implies the L^2 -norm. R and λ are the regularization matrix and parameter, respectively. The two regularizers used in the GUI are the Tikhonov regularization ($R = I$, with I being the identity matrix) and the Laplacian regularization ($R = L$, with L being the incidence matrix; construction of the incidence matrix L is detailed in the Appendix). The solution to the optimization problem in Eq. (4) is

$$\hat{\underline{h}} = (M^T M + \lambda^2 R^T R)^{-1} M^T \underline{p}_{\text{meas}}. \quad (5)$$

To avoid the computation and storage burden associated with solving Eq. (5), the GUI uses MATLAB’s “lsqr” function to solve Eq. (4) iteratively, directly computing $\{M\underline{u}$ and $M^T\underline{v}\}$ instead of constructing/using M explicitly. Here, u is a vector of size $(N \times 1)$, while v is a vector of size $(N_d \cdot N_t \times 1)$. These vectors are updated during the LSQR iterations which employ Mu and $M^T v$ evaluations to calculate the updated u and v vectors.

For efficient evaluation of $M\underline{u}$ and $M^T\underline{v}$ during the iterations, certain quantities [\tilde{E} (contributing triangular elements), \tilde{N} (corresponding finite-element basis functions), and \tilde{T} (corresponding time samples)] for all the detectors are computed beforehand,³⁵ and used throughout the LSQR minimization. The GUI also provides the noniterative, MBP reconstruction, characterized by⁴⁰

$$\hat{\underline{h}} = M^T \underline{p}_{\text{meas}}. \quad (6)$$

2.2. Methods used in preparing the GUI

The graphical user interface application was created through MATLAB’s 2021a GUI Development Environment (GUIDE) toolkit and a built-in MATLAB application compiler. The interface utilizes multiple text edit classes for user input and static edit classes for easy-to-read code feedback. A series of callback functions are strung together to collect user data and specifications upon entry for further computation after select pushbuttons are activated. User-determined MATLAB files and text inputs are called into a local variable before being stored in the UI globally as an hObject within the handles structure, allowing them to pass from function to function. Instantiations of the global variables are created before use in parallel

for loops, which are employed for accelerated reconstructions.

All text inputs activate a callback function for retrieval before reconstruction begins. For ease of use, initial computation begins once the user confirms their inputs, permitting the user to change inputs whenever they want without laboriously re-entering every other value. In all regions where the code may take more than a couple of seconds to run, a loading display is created using a “uifigure” to inform the user that the application is still running. A display button for each of the three reconstructions, namely BP, MBP, and LSQR reconstruction, needs to be selected before each reconstruction method’s code is performed and the triangular surface plot (trisurf) is displayed.

The algorithm demonstrated in Sec. 2.1 is employed for evaluating the MB reconstructions. The region of interest (ROI) is first discretized using the Delaunay triangulation function. Therefore the domain size and grid resolution, and the number of quadrature points for evaluating the integrals in Eq. (3) must be chosen by the user. Before performing the MB image reconstructions, the GUI performs pre-computation of the quantities $\tilde{E}\{i_d = 1, \dots, N_d\}$, $\tilde{N}\{i_d = 1, \dots, N_d\}$, and $\tilde{T}\{i_d = 1, \dots, N_d\}$ and stores them. The pre-computed quantities are then used to evaluate the model-based reconstructions efficiently.

3. Results and Discussion

3.1. The GUI and its components

Upon launching the “Image_Reconstruction_2D” application, the window shown in Fig. 2 appears displaying two main panels: one for user inputs and the other for three different reconstruction outputs: BP, MBP, and LSQR reconstruction.

The top panel includes both mandatory and optional inputs while the bottom panel exhibits three different types of image reconstruction plots and a text box for possible errors in the inputs that would cause an unclear plot or stalled code.

To optimize intuitive usage, text boxes are disabled until a user specifies the type of input they desire and serve to guide the user through the input panel for smooth operation. An additional text figure on the bottom of the output panel functions to warn users of missing or incompatible inputs as well as provide additional information for possible problems in the reconstruction.



Fig. 2. The appearance of the RACT2D GUI.

3.1.1. Measurements and detection geometry inputs

The panel for loading the detection geometry and measurement data is shown in Fig. 3(a), and the corresponding excerpts from the code are shown in Figs. 3(b)–3(d). To use the GUI, the user must have a discrete XA/PA data received by the ultrasonic transducers in the form of a .mat file and the sampling frequency used. For proper functioning of the GUI, the data should be in the form of a matrix with dimensions $N_d \times N_t$, with N_d and N_t being the number of detectors and the number of time samples acquired at the sampling rate/frequency F_s , respectively. The main components for defining the detection geometry are the region of interest (which includes the excitation area and where the reconstruction is desired) and the location of the detector

elements with respect to the ROI. For simplicity, the ROI is chosen to be a rectangle and the detection coordinates need to be calculated considering the center of the ROI as the origin. The detector coordinates should be loaded by the user as a .mat file consisting of a matrix of dimensions $N_d \times 2$, where the two columns carry the x - and y -coordinates of the detectors. For the ease of the users, if the measurements were made using a ring array, they only need to provide its radius. The next input is the speed of sound propagation in the medium, which is needed for time-of-flight calculations in the reconstruction algorithms. The ROI is discretized into a regular finite-element grid and the user needs to provide the grid resolution. Choice of grid resolution is a crucial aspect in deciding the computational efficiency and the reconstruction results.

The screenshot shows a GUI window titled 'Sensor Data'. It contains a text input field for the sensor data file name and a 'Browse Sensor Data' button. Below this, there are three main sections: 'Reconstruction Area (m)' with input fields for 'x length', 'y length', and 'grid resolution'; 'Variables' with input fields for 'medium sound speed (m/s)' and 'sampling frequency (Hz)'; and 'Detector Array' with radio buttons for 'Ring Array' and 'Other Array', a 'Radius (m)' input field, and a 'Browse Detectors' button.

(a)

```
% Defining the Region of interest
Grid.X = 2.5e-2; Grid.Y = 2.5e-2; %size of domain of interest [in m]
Grid.h = 1e-3/8; % Grid resolution [m]
% Domain discretization
[Grid.cords,Grid.tri] = Triangulation2D(Grid.X,Grid.Y,Grid.h);
```

(b)

```
% Defining Detector Geometry:-----
% 128 elements placed on a circle of radius [5.0cm]
r_det = 5e-2; d_theta=2*pi/128;
Det.cords = r_det*[cos([0:d_theta:2*pi-d_theta])', sin([0:d_theta:2*pi-d_theta])'];
% *** users may also load a .mat file with the detector co-ordinates in a
% matrix of size (# of detecors x 2). Column 1&2: x&y co-ordinates ***
Det.Fs=20e6;
vs = 1500; % speed of sound in medium [m/s]
Det.t_mat = TimeVector(Grid.cords,Det,vs);
```

(c)

```
% Load Data [a matrix of size: # of detectors x # of time samples]
load('D:\Prabodh\RACT2D_CodesJune2022\Data\P_mmt_blood_vessel_20MHz_128ele_ring.mat')
P_mat= P_mat_data; % [size: 128 x 1082]
```

(d)

Fig. 3. (a) Input panel of the GUI; and excerpts from the shared code for (b) defining the ROI, (c) defining the detection geometry, and (d) loading the RA measurement dataset to be used for reconstructions.

It should be chosen small enough so that it is able to represent the thinnest structures expected in the ROI, but a very small grid resolution adversely affects the reconstruction speed and may also lead to “Out of Memory” error.

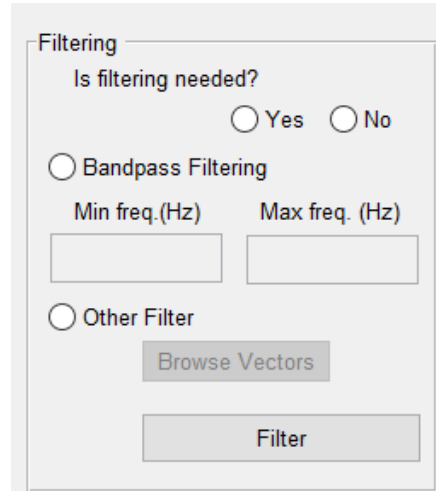
3.1.2. Filtering

Before passing the data to the reconstruction algorithms, filtering of the signals is often desired, especially for any noisy high-frequency components of the signal. The toolbox offers bandpass filtering (by defining the maximum and minimum frequencies in the band) as well as filtering using a user-defined filter, to be provided as input in the GUI [Fig. 4(a)];

the corresponding excerpt from the code is provided in Fig. 4(b), and the effect of filtering is demonstrated in Fig. 4(c).

3.1.3. Parameters for model-based reconstructions

The MB algorithm used by the GUI is based on our recent work.³⁶ For performing MB reconstructions, quadrature points for computing the circular line integral in Eq. (3) for evaluating the elements of the matrix M and a regularization parameter to compute the regularized LSQR reconstruction are needed. While the users may choose their own values for these two parameters, the default value of



(a)

```
% ***** Signal Filtering *****
Filt.choice='No'; % No/custom/bandpass

if strcmp(Filt.choice,'bandpass')==1
    disp('User input: frequencies Fc1 and Fc2 [Hz] for the frequency band')
    Fc1=1e6; % lower limit (<= Fs/2)
    Fc2=5e6; % upper limit (<= Fs/2)
    Filt.filt=BandPassFilter(Fc1,Fc2,Det.Fs,P_mat);
elseif strcmp(Filt.choice,'custom')==1
    disp('User input: Loading a filtering vector');
    Filt.filt=custom_filter; % vector of size [# of time samples/2 x 1]
end

if strcmp(Filt.choice,'bandpass')==1 || strcmp(Filt.choice,'custom')==1
    P_mat=Sigfiltering(Filt.filt,P_mat);
else
    disp('No filtering done')
end
```

(b)

Fig. 4. (a) Signal filtering panel of the GUI, (b) the piece of MATLAB code for performing the filtering, and (c) an illustration of filtering of a typical RA signal.

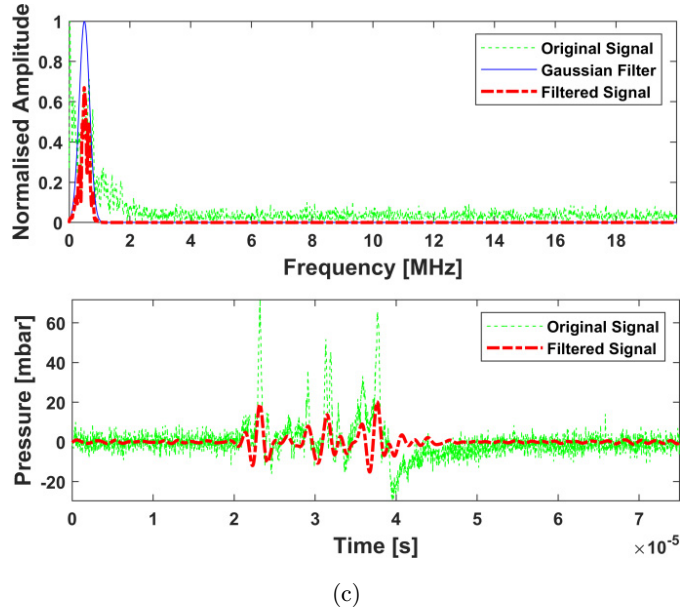
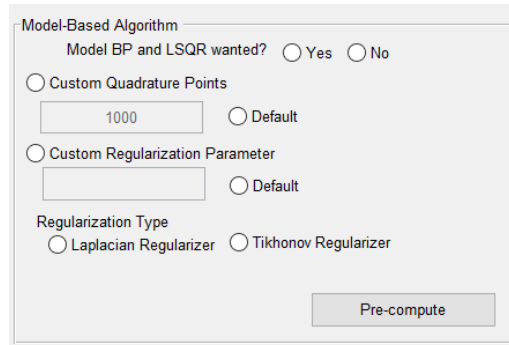


Fig. 4. (Continued)

the number of quadrature points is 1000, and the default regularization parameter is $\|p_{\text{meas}}\|^2/N$ with N being the total number of nodes in the reconstruction domain. Figure 5(a) demonstrates the

GUI panel where the users have to provide the parameters needed to perform the MB reconstruction. The corresponding excerpt from the code is provided in Fig. 5(b) and the codes for



(a)

```

% Parameters for Model-based reconstructions
Model.quad = 1000;
Model.lambda = 1e22; %
Model.Reg = 'Laplacian' ; %Laplacian/None/Tikhonov
if strcmp(Model.Reg, 'Laplacian')==1
[Lap,Inc] = makeLaplacian(Grid);
Model.RegMat=Inc;
elseif strcmp(Model.Reg, 'Tikhonov')==1
    Model.RegMat=speye(size(Grid.cords,1));
else
    disp('No regularization')
    Model.RegMat=[];
end
    
```

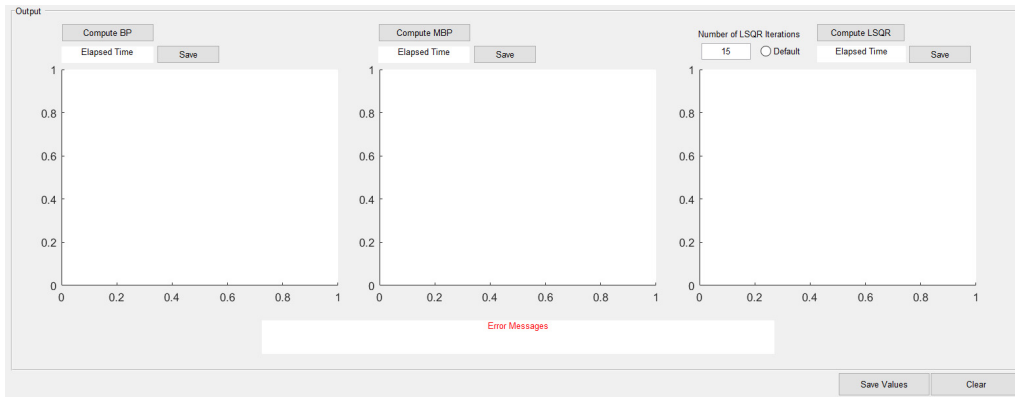
(b)

```

% ***** PreComputed variables *****
% PreComp.E,PreComp.N,PreComp.T
% [Pandey et al, IEEE TUFFC 68.12 (2021)]
PreComp=Precomputing(Grid,Det,vs,model.quad);
% MBP Reconstruction
rec.MBP=MBPEval(Grid,Det,model,PreComp,vs,P_mat);
% MF-LSQR reconstruction
A_sysmat_m = @(x) RegMtMuProdFn(x,Grid,Det,model,PreComp,vs);
rec.MFLSQR =gmres(A_sysmat_m,rec.MBP(:),[],1e-6,10);
    
```

(c)

Fig. 5. Inputs for model-based reconstructions in the (a) GUI, (b) MATLAB code, and (c) the code for evaluating the MBP and MF-LSQR reconstructions.



(a)

```

% Visualizing the reconstructions
Grid.tri1=Grid.tri(:,:,);
figure, trisurf(Grid.tri1,Grid.cords(:,1),Grid.cords(:,2),rec.BP(:)); shading interp;
axis tight
title('BP reconstruction');
view([0 90]), colormap(hot)
figure, trisurf(Grid.tri1,Grid.cords(:,1),Grid.cords(:,2),rec.MBP(:)); shading interp;
axis tight
title('MBP reconstruction');
view([0 90]), colormap(hot)
figure, trisurf(Grid.tri1,Grid.cords(:,1),Grid.cords(:,2),rec.MFLSQR(:)); shading interp;
axis tight
title('MF-LSQR reconstruction');
view([0 90]), colormap(hot)

```

(b)

Fig. 6. (a) Display panel of the GUI and (b) the piece of code for viewing the reconstructions.

pre-computing the quantities $\{\tilde{E}, \tilde{N}, \tilde{T}\}$ and evaluating the MBP and MF-LSQR reconstructions are shown in Fig. 5(c). The panel displaying the reconstructed images in the GUI is shown in Fig. 6(a) and the code for viewing these images is provided in Fig. 6(b). In order to evaluate the MB reconstructions, the user needs to provide the number of quadrature points on the arc for computing the integral in Eq. (3). A compiled list with an explanation of each input variable can be found in Table 1.

3.2. Datasets included in the GUI and reconstruction results

To display the capabilities of the application, a demo synthetic and an experimental RACT dataset have been included with the GUI. The synthetic data was generated from a vascular-shaped RED map [Fig. 1(b)] and the experimental XACT data was obtained from a gelatin-based phantom with a T-shaped target as shown in Fig 1(c). The detector

grid is a circular array with 128 equally spaced elements and 5-cm radius, concentric with the RED. The detector coordinates are stored in a .mat file labeled “DetCords5cmRingArray.mat”. Synthetic RA data were computed at spatial resolution $h = 0.03$ mm and sampling frequency $F_s = 20$ MHz, with quadrature points $N_q \approx 2000$ using the model from Eq. (3).

For performing the reconstruction in the GUI, the ROI was chosen as a $2.5 \text{ cm} \times 2.5 \text{ cm}$ square with a grid resolution of 0.2 mm. Sound speed in the medium was kept at 1500 m/s, which is the same speed as in water and soft tissue. For MBP and LSQR, the quadrature points and the regularization parameter were kept at the default values. The BP, MBP, and MF-LSQR reconstructions using the complete-frequency BW are shown in Fig. 7(a). The reconstructions from 0–2-MHz and 0–5-MHz bandpass-filtered signals are shown in Figs. 7(b) and 7(c), respectively. Figure 7(d) demonstrates the reconstructions obtained from signals after being filtered using the provided user-defined Gaussian

Table 1. List of inputs.

| Input variable(s) | Variable(s) in code | Format/unit | Data type | Comments |
|--|---------------------|---|--------------|--|
| x -length, y -length | Grid.X, Grid.Y | m | Double | Determine the entire length of the reconstruction area's x - and y -axes |
| Grid resolution | Grid.h | m | Double | Determines the pixel size |
| Medium sound speed | vs | m/s | Double | The material property of the medium of acoustic propagation. The default medium for demonstrations has been water/soft tissues at 1500 m/s |
| Sampling frequency | Det.Fs | Hz | Double | Number of samples taken by the transducers in a second |
| Transducers — Ring array radius | r_det | m | Double | Determines the radius of a ring array. The radius should be greater than the radius of the circumcircle to the reconstruction area |
| Transducers — Unique array | Det.cords | .mat file, size: number of transducers \times 2 | Double | For any other unique transducer array pattern. Each row carries the x - and y -coordinates of a transducer |
| Bandpass filtering — Min and max frequencies | Filt.Fc1, Filt.Fc2 | Hz | Double | Maximum filtering frequency should not exceed half of the sampling frequency |
| Unique filtering vector | Filt.filt | User-defined.mat file | Double | For any unique filtering vector |
| Quadrature points | Model.quad | | Double | Number of quadrature points, default value is 1000 |
| Regularization parameter | Model.lambda | | Double | Default value: $\ p_{\text{meas}}\ ^2/N$; N is the total number of nodes in the ROI |
| Type of regularization | Model.Reg | | Radio button | Laplacian or Tikhonov |

filter (filename: “filt_3MHz_80BW_Gaussian.mat”, central frequency: 3 MHz, and FWHM: 2.4 MHz). The correlation of the reconstructions with respect to the true phantom was evaluated to quantify the reconstruction accuracy and provided at the bottom of each image (only in this paper; not part of the GUI). The BP and MBP in all the test cases have low correlation coefficients because these algorithms only provide the structural information and the reconstructed images lack the quantitative information. The MF-LSQR algorithm on the other hand is a quantitative reconstruction algorithm and hence yields high correlation values. Among all the MF-LSQR reconstructions, the one corresponding to 2-MHz low-pass filtering has the highest correlation because it omits the high-frequency fluctuations and yields a smooth image of the target.

The second dataset shared with the GUI was obtained from an XACT experiment using a 128-element ring array transducer (radius: 5 cm)

with 5-MHz central frequency ($\geq 60\%$ bandwidth) at 40-MHz sampling frequency. A T-shaped lead target was positioned near the center of a gelatin phantom. The phantom was concentric with the ring array and the setup was placed in a water tank and 30-ns X-ray pulses were used to irradiate the phantom. For more experimental details, readers may refer to Sec. IV in Ref. 36. Figure 8 displays the reconstruction results obtained from the BP, MBP, and LSQR algorithms using the XACT data. The quality of the reconstructions is quantified via the contrast-to-noise ratio (CNR). The target region is chosen as the smaller square and the background region is chosen as the large rectangle as marked in the LSQR image of Fig. 8. The CNR values for each of these reconstructions are provided at the bottom of the respective images (only in this paper; not part of the GUI). As expected, the MF-LSQR algorithm reduces the noisy artifacts in the reconstructed image and hence yields the highest CNR, while the performances of BP and MBP are comparable.

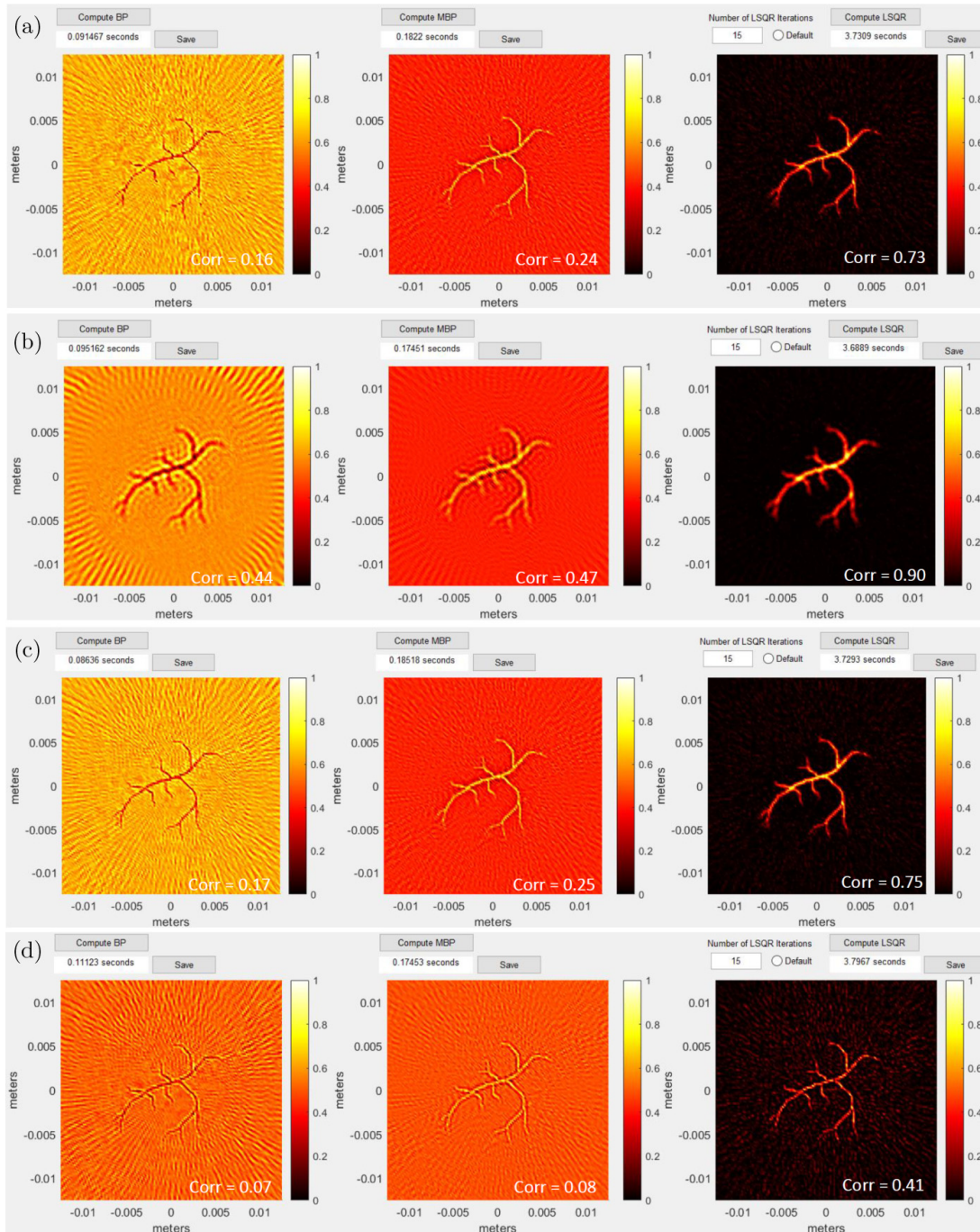


Fig. 7. Reconstructions of the vascular structure with (a) full-frequency BW, (b) 0–2-MHz and (c) 0–5-MHz bandpass-filtered signals, and (d) Gaussian-filtered (central frequency: 3 MHz, FWHM: 2.4 MHz) signal. First column: BP, second column: MBP, and third column: LSQR.

3.2.1. Saving the reconstructed results and data

In the display panel presented in Fig. 6, a save button is available to save each individual plot (including the color bar and axes) as an image file. The variables computed during the reconstructions,

which are needed to visualize and further process the images, can also be exported as an external MATLAB file. The variables which are stored are tabulated in Table 2.

A text box above each of the reconstruction plot displays the time taken in evaluating it. The images

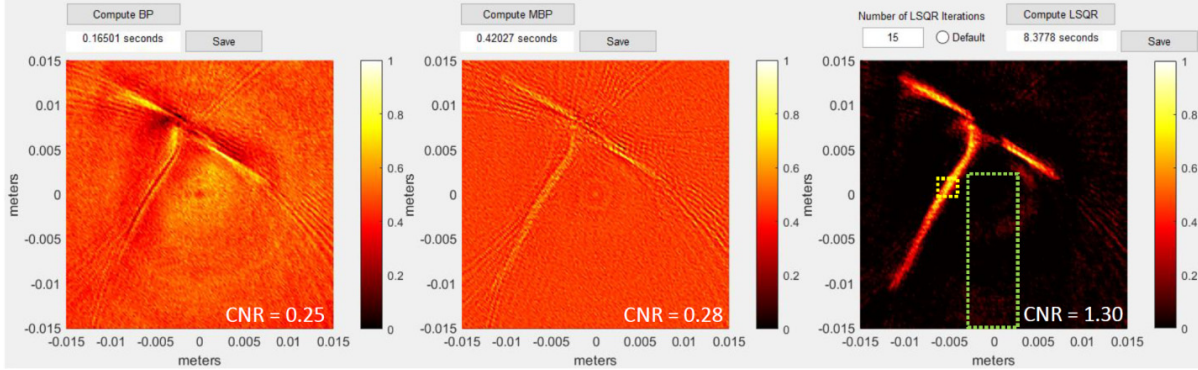


Fig. 8. Reconstructions from experimental XACT data. First column: BP, second column: MBP, and third column: LSQR.

Table 2. The saved variables in the GUI.

| Saved variable | Function |
|----------------|---|
| Grid.cords | The x - and y -coordinates of all the nodes in the reconstruction domain |
| Grid.tri | Delaunay triangulation from the points in a matrix p.d. tri.d is a three-column matrix where each row contains the row indices of the input points that make up a triangle in the triangulation |
| Grid.h | Grid resolution |
| Filt | The filter used for signal processing |
| Rec.BP | BP reconstruction (size: Nodes.d \times 1) |
| Rec.LSQR | LSQR reconstruction (size: Nodes.d \times 1) |
| Rec.MBP | MBP reconstruction (size: Nodes.d \times 1) |

The reconstructed image can be viewed in MATLAB using the following command: `figure, trisurf(Grid.tri, Grid.cords(:,1), Grid.cords(:,2), Rec.LSQR); shading interp.`

demonstrated in this paper were computed on a workstation with an AMD Ryzen™ Threadripper™ 3960X 24-core processor (3.79 GHz) with 256-GB RAM. The reconstruction algorithms were written to enable the cores to perform the computations in parallel.

3.2.2. Discussion

The term MBP was first reported by Ding *et al.*⁴⁰ Although the name includes the term “back-projection”, the operator corresponding to MBP evaluation given in Algorithm 2 of our previous work³⁵ is computationally more involving than BP, and hence takes longer to evaluate the reconstructions. The matrix-free evaluation of the LSQR minimizer enables to compute 2D and 3D reconstructions with low memory demands. The GUI and codes demonstrated in this paper correspond to the 2D reconstructions only. The work on the model-based 3D reconstruction algorithms is ongoing. Moreover, this work does not include GPU

acceleration. Future work will be focused on GPU-accelerated evaluations of 2D and 3D reconstructions. While the MB algorithms are computationally demanding, enabling parallel computation significantly reduces the computation time. All the algorithms used in the GUI are executed on the CPU only. The BP algorithm being computationally straightforward can easily be accelerated using GPUs. Efforts on GPU acceleration of the BP and MB algorithms are ongoing, and we expect the future versions to include the GUI computation capability.

Recently, Hofmann *et al.*⁵⁶ showed that the model-matrix from experimental calibration measurements can incorporate several experimental attributes such as detector spatial response, sound-speed variations, acoustic attenuation, etc. Therefore, such a model-matrix is expected to improve the reconstruction quality. At present, our GUI does not offer the flexibility to incorporate such a model-matrix, but it will be included in the future release of the GUI. In our recent work,⁵⁷ we

demonstrated model-based 3D XACT reconstructions and the future version of GUI will also have the 3D reconstruction capability.

4. Conclusion

Radiation-induced acoustic tomographic problems aim to reconstruct the radiation energy deposition in the tissue, from boundary acoustic measurements. While the traditional back-projection algorithm is easy to implement, it carries noise and limited-view artifacts. The model-based algorithms are mathematically rigorous and computationally demanding but are known to ameliorate these artifacts. We developed an easy-to-use GUI that facilitates the users to perform traditional BP and model-based 2D image reconstructions simply by clicking a button. In this paper, we demonstrated the use of the developed GUI using numerical and experimental XACT datasets. The algorithms enable using the cores of the computer to evaluate the reconstructions in parallel, thus making the computations more efficient.

Acknowledgments

This work was supported by the National Institute of Health (R37CA240806) and American Cancer Society (133697-RSG-19-110-01-CCE). The authors would like to acknowledge the support from UCI Chao Family Comprehensive Cancer Center (P30CA062203). The authors would also like to thank Kristina and Kaitlyn for proofreading the paper.

Conflicts of Interest

The authors declare that there are no conflicts of interest relevant to this article.

Appendix A.

The incidence matrix B is of the size = number of edges \times number of nodes in the discretized domain. The elements of this matrix are defined as

$$B_{ij} = \begin{cases} -1 & \text{if edge } e_j \text{ leaves vertex } v_i, \\ 1 & \text{if edge } e_j \text{ enters vertex } v_i, \\ 0 & \text{otherwise.} \end{cases}$$

References

1. L. Xiang, B. Han, C. Carpenter, G. Pratz, Y. Kuang, L. Xing, "X-ray acoustic computed tomography with pulsed X-ray beam from a medical linear accelerator," *Med. Phys.* **40**(1), 010701 (2013).
2. E. Robertson, L. Xiang, "Theranostics with radiation-induced ultrasound emission (TRUE)," *J. Innov. Opt. Health Sci.* **11**(03), 1830002 (2018).
3. P. Samant, L. Trevisi, X. Ji, L. Xiang, "X-ray induced acoustic computed tomography," *Photoacoustics* **19**, 100177 (2020).
4. S. Wang, Radiation-induced acoustic imaging system development and application, M.S. Thesis, The University of Oklahoma, Norman, Oklahoma (2019).
5. L. Xiang, S. Tang, M. Ahmad, L. Xing, "High resolution X-ray-induced acoustic tomography," *Sci. Rep.* **6**(1), 26118 (2016).
6. S. Tang, D. H. Nguyen, A. Zarafshani, C. Ramseyer, B. Zheng, H. Liu, L. Xiang, "X-ray-induced acoustic computed tomography with an ultrasound transducer ring-array," *Appl. Phys. Lett.* **110**(10), 103504 (2017).
7. C. H. Kim *et al.*, U.S. Patent Application No. 16/488236 (2019).
8. S. Choi, D. Lee, E. Y. Park, J. J. Min, C. Lee, C. Kim, "3D X-ray induced acoustic computed tomography: A phantom study," *Proc. SPIE* **11240**, 286–289 (2020).
9. J. Xia, J. Yao, L. V. Wang, "Photoacoustic tomography: Principles and advances," *Prog. Electromagn. Res.* **147**, 1–22 (2014).
10. A. Hauptmann, B. T. Cox, "Deep learning in photoacoustic tomography: Current approaches and future directions," *J. Biomed. Opt.* **25**(11), 112903 (2020).
11. X. Wang, W. W. Roberts, P. L. Carson, D. P. Wood, J. B. Fowlkes, "Photoacoustic tomography: A potential new tool for prostate cancer," *Biomed. Opt. Express* **1**(4), 1117–1126 (2010).
12. X. Wang, Y. Pang, G. Ku, X. Xie, G. Stoica, L. V. Wang, "Noninvasive laser-induced photoacoustic tomography for structural and functional *in vivo* imaging of the brain," *Nat. Biotechnol.* **21**(7), 803–806 (2003).
13. S. Liu, Z. Zhao, Y. Lu, B. Wang, Z. Nie, Q. H. Liu, "Microwave induced thermoacoustic tomography based on probabilistic reconstruction," *Appl. Phys. Lett.* **112**(26), 263701 (2018).
14. Y. Cui, C. Yuan, Z. Ji, "A review of microwave-induced thermoacoustic imaging: Excitation source, data acquisition system and biomedical applications," *J. Innov. Opt. Health Sci.* **10**(04), 1730007 (2017).

15. M. Aliroteh, H. Nan, A. Arbabian, Microwave-induced thermoacoustic tomography for subcutaneous vascular imaging, *Proc. 2016 IEEE Int. Ultrasonics Symp. (IUS)*, pp. 1–4 (2016).
16. X. Jin, Microwave-induced thermoacoustic tomography: Applications and corrections for the effects of acoustic heterogeneities, Ph.D. Thesis, Texas A&M University (2007).
17. K. C. Jones, A. Witztum, C. M. Sehgal, S. Avery, “Proton beam characterization by proton-induced acoustic emission: Simulation studies,” *Phys. Med. Biol.* **59**(21), 6549–6563 (2014).
18. S. Kellnberger et al., “Ionoacoustic tomography of the proton Bragg peak in combination with ultrasound and optoacoustic imaging,” *Sci. Rep.* **6**(1), 29305 (2016).
19. K. Parodi, W. Assmann, “Ionoacoustics: A new direct method for range verification,” *Mod. Phys. Lett. A* **30**(17), 1540025 (2015).
20. C. Freijo, J. L. Herraiz, D. Sanchez-Parcerisa, J. M. Udias, “Dictionary-based protoacoustic dose mapping for proton range verification,” *Photoacoustics* **21**, 100240 (2021).
21. L. V. Wang, H. I. Wu, *Biomedical Optics: Principles and Imaging*, John Wiley & Sons (2012).
22. R. Baskar, K. A. Lee, R. Yeo, K. W. Yeoh, “Cancer and radiation therapy: Current advances and future directions,” *Int. J. Med. Sci.* **9**(3), 193–199 (2012).
23. B. Schaffner, E. Pedroni, “The precision of proton range calculations in proton radiotherapy treatment planning: Experimental verification of the relation between CT-HU and proton stopping power,” *Phys. Med. Biol.* **43**(6), 1579–1592 (1998).
24. S. Hickling, P. Léger, I. El Naqa, Simulation and experimental detection of radiation-induced acoustic waves from a radiotherapy linear accelerator, *Proc. 2014 IEEE Int. Ultrasonics Symp.*, pp. 29–32 (2014).
25. S. Hickling, M. Hobson, I. El Naqa, “Feasibility of X-ray acoustic computed tomography as a tool for noninvasive volumetric in vivo dosimetry,” *Int. J. Radiat. Oncol. Biol. Phys.* **90**(1_Suppl.), S843 (2014).
26. S. Hickling, P. Léger, I. El Naqa, “On the detectability of acoustic waves induced following irradiation by a radiotherapy linear accelerator,” *IEEE Trans. Ultrason. Ferroelectr. Freq. Control* **63**(5), 683–690 (2016).
27. J. Kim et al., “X-ray acoustic-based dosimetry using a focused ultrasound transducer and a medical linear accelerator,” *IEEE Trans. Radiat. Plasma Med. Sci.* **1**(6), 534–540 (2017).
28. F. Forghani et al., “Simulation of X-ray-induced acoustic imaging for absolute dosimetry: Accuracy of image reconstruction methods,” *Med. Phys.* **47**(3), 1280–1290 (2020).
29. S. Hickling et al., “Ionizing radiation-induced acoustics for radiotherapy and diagnostic radiology applications,” *Med. Phys.* **45**(7), e707–e721 (2018).
30. E. Lens, A. de Blécourt, D. Schaart, F. Vos, K. van Dongen, “OC-0567: Reconstructing the 3-D proton dose distribution from the modelled iono-acoustic wave field,” *Radiother. Oncol.* **133**, S297–S298 (2019).
31. D. Lee, E. Y. Park, S. Choi, H. Kim, J. J. Min, C. Lee, C. Kim, “GPU-accelerated 3D volumetric X-ray-induced acoustic computed tomography,” *Biomed. Opt. Express* **11**(2), 752–761 (2020).
32. Y. Li, P. Samant, S. Wang, A. Behrooz, D. Li, L. Xiang, “3-D X-ray-induced acoustic computed tomography with a spherical array: A simulation study on bone imaging,” *IEEE Trans. Ultrason. Ferroelectr. Freq. Control* **67**(8), 1613–1619 (2020).
33. E. Robertson, P. Samant, S. Wang, T. Tran, X. Ji, L. Xiang, “X-ray-induced acoustic computed tomography (XACT): Initial experiment on bone sample,” *IEEE Trans. Ultrason. Ferroelectr. Freq. Control* **68**(4), 1073–1080 (2020).
34. S. Choi, E. Y. Park, S. Park, J. H. Kim, C. Kim, “Synchrotron X-ray induced acoustic imaging,” *Sci. Rep.* **11**(1), 4047 (2020).
35. P. K. Pandey, S. Wang, H. O. Aggrawal, K. Bje-govic, S. Boucher, L. Xiang, “Model-based X-ray-induced acoustic computed tomography,” *IEEE Trans. Ultrason. Ferroelectr. Freq. Control* **68**(12), 3560–3569 (2021).
36. P. K. Pandey, S. Wang, L. Xiang, “Model-based reconstruction algorithm for X-ray induced acoustic tomography,” *Proc. SPIE* **11595**, 1004–1010 (2021).
37. S. Wang, V. Ivanov, P. K. Pandey, L. Xiang, “X-ray-induced acoustic computed tomography (XACT) imaging with single-shot nanosecond X-ray,” *Appl. Phys. Lett.* **119**(18), 183702 (2021).
38. M. Xu, L. V. Wang, “Universal back-projection algorithm for photoacoustic computed tomography,” *Phys. Rev. E* **71**(1), 016706 (2005).
39. A. Buehler, A. Rosenthal, T. Jetzfellner, A. Dima, D. Razansky, V. Ntziachristos, “Model-based optoacoustic inversions with incomplete projection data,” *Med. Phys.* **38**(3), 1694–1704 (2011).
40. L. Ding, D. Razansky, X. L. Deán-Ben, “Model-based reconstruction of large three-dimensional optoacoustic datasets,” *IEEE Trans. Med. Imaging* **39**(9), 2931–2940 (2020).
41. P. K. Pandey, H. O. Aggrawal, S. Wang, K. Kim, A. Liu, L. Xiang, “Ring artifacts removal in X-ray-induced acoustic computed tomography,” *J. Innov. Opt. Health Sci.* **15**(03), 2250017 (2022).
42. A. Rosenthal, T. Jetzfellner, D. Razansky, V. Ntziachristos, “Efficient framework for model-based

- tomographic image reconstruction using wavelet packets,” *IEEE Trans. Med. Imaging* **31**(7), 1346–1357 (2012).
43. C. Lutzweiler, X. L. Deán-Ben, D. Razansky, “Expediting model-based optoacoustic reconstructions with tomographic symmetries,” *Med. Phys.* **41**(1), 013302 (2014).
 44. L. Ding, X. L. Deán-Ben, C. Lutzweiler, D. Razansky, V. Ntziachristos, “Efficient non-negative constrained model-based inversion in optoacoustic tomography,” *Phys. Med. Biol.* **60**(17), 6733 (2015).
 45. Y. Han, S. Tzoumas, A. Nunes, V. Ntziachristos, A. Rosenthal, “Sparsity-based acoustic inversion in cross-sectional multiscale optoacoustic imaging,” *Med. Phys.* **42**(9), 5444–5452 (2015).
 46. L. Ding, X. L. Deán-Ben, C. Lutzweiler, D. Razansky, V. Ntziachristos, “Image reconstruction in cross-sectional optoacoustic tomography based on non-negative constrained model-based inversion,” *Proc. SPIE* **9539**, 953919 (2015).
 47. L. Ding, X. L. Deán-Ben, D. Razansky, “Real-time model-based inversion in cross-sectional optoacoustic tomography,” *IEEE Trans. Med. Imaging* **35**(8), 1883–1891 (2016).
 48. C. Lutzweiler, S. Tzoumas, A. Rosenthal, V. Ntziachristos, D. Razansky, “High-throughput sparsity-based inversion scheme for optoacoustic tomography,” *IEEE Trans. Med. Imaging* **35**(2), 674–684 (2015).
 49. X. L. Deán-Ben, E. Merčep, D. Razansky, “Hybrid-array-based optoacoustic and ultrasound (OPUS) imaging of biological tissues,” *Appl. Phys. Lett.* **110**(20), 203703 (2017).
 50. X. L. Deán-Ben, L. Ding, D. Razansky, “Dynamic particle enhancement in limited-view optoacoustic tomography,” *Opt. Lett.* **42**(4), 827–830 (2017).
 51. S. Biton, N. Arbel, G. Drozdov, G. Gilboa, A. Rosenthal, “Optoacoustic model-based inversion using anisotropic adaptive total-variation regularization,” *Photoacoustics* **16**, 100142 (2019).
 52. H. Yang *et al.*, “Soft ultrasound priors in optoacoustic reconstruction: Improving clinical vascular imaging,” *Photoacoustics* **19**, 100172 (2020).
 53. D. O’Kelly *et al.*, “A scalable open-source MATLAB toolbox for reconstruction and analysis of multispectral optoacoustic tomography data,” *Sci. Rep.* **11**(1), 19872 (2021).
 54. J. Jiang, A. Kalyanov, L. Ahnen, S. Lindner, A. Di Costanzo Mata, M. Wolf, S. Sánchez Majos, A new method based on virtual fluence detectors and software toolbox for handheld spectral optoacoustic tomography, *Oxygen Transport to Tissue XL*, Advances in Experimental Medicine and Biology, pp. 357–361, Springer, Cham (2018).
 55. P. Omid, L. C. M. Yip, E. Rascevska, M. Diop, J. J. L. Carson, “PATLAB: A graphical computational software package for photoacoustic computed tomography research,” *Photoacoustics* **28**, 100404 (2022).
 56. U. A. Hofmann, W. Li, X. L. Deán-Ben, P. Subochev, H. Estrada, D. Razansky, “Enhancing optoacoustic mesoscopy through calibration-based iterative reconstruction,” *Photoacoustics* **28**, 100405 (2022).
 57. P. K. Pandey, S. Wang, L. Sun, L. Xing and L. Xiang, “Model-based Three-dimensional X-ray induced acoustic computerized tomography,” in *IEEE Transactions on Radiation and Plasma Medical Sciences*, doi: 10.1109/TRPMS.2023.3238017.